49th AIAA Aerospace Sciences Meeting including the New Horizons Forum and Aerospace Exposition
4 - 7 January 2011, Orlando, Florida

AIAA 2011-283

Instability and Transition Research in a Mach-6 Quiet Tunnel

Amanda Chou*, Bradley M. Wheaton*, Christopher A. C. Ward*,
Peter L. Gilbert*, Laura E. Steen*, and Steven P. Schneider†
School of Aeronautics and Astronautics, Purdue University, West Lafayette, IN 47907-1282

Pitot-probe measurements were made to determine the spatial extent of the uniform quiet flow core for the laminar nozzle-wall boundary layer. The uniformity of the flow for a turbulent nozzle-wall boundary layer was determined as well. The nozzle was re-polished in August, and quiet flow is currently being achieved at higher stagnation pressures, around 162 psia. The laser perturber system for the BAM6QT is being re-established. The laser used for this system performs as in previous experiments and a new optical system has been designed for the BAM6QT.

Tests were conducted to characterize the effect of suction downstream of the nozzle exit on starting larger blunt models in hypersonic flow. Pressure measurements were made in the upstream pipe-insert section and found that suction levels were highest with a 0.375-in. gap. Models of the Crew Exploration Vehicle (CEV) with diameters of 1.000 and 1.250 in. started regardless of model positioning and gap suction. A 1.500-in. model started in quiet flow, but did not start in noisy flow with pipe-insert suction alone. The 1.500-in. CEV model did, however, start in noisy flow with bleeds open above the maximum quiet pressure. Another project looked at the effect of nosetip roughness on the crossflow instability with a 7-deg half-angle cone at 6-deg angle of attack. When the average roughness of the nosetip was varied by an order of magnitude, the temperature-sensitive paint data showed no effect on the stationary vortices. It appears that the paint step at the nosetip-frustum junction was dominating the generation of the stationary vortices. Lastly, measurements upstream of a cylindrical roughness have confirmed the existence of an absolute instability in the separation region, as suggested by computations. A second absolute instability was also detected at lower Reynolds numbers.

Nomenclature

D	diameter
δ	boundary layer thickness
k	roughness height
p	pressure
Δp	pressure differential
$\dot{q}$	heat flux
Re	Reynolds number
Re_k	Reynolds number based on roughness height
t	time after tunnel start
T	temperature
ΔT	change in temperature
ρ	density
x	spanwise distance from center of roughness element on wall, at wall
y	height above the nozzle wall
z	distance from tunnel throat

*Research Assistant, Student Member AIAA
†Professor, Associate Fellow AIAA

z_0	nozzle-wall roughness element location

Subscript

0	at stagnation conditions
1	conditions before a shock
i	at initial conditions

Abbreviations

AO	acoustic origin
BAM6QT	Boeing/AFOSR Mach-6 Quiet Tunnel
CEV	Crew Exploration Vehicle
FFT	fast Fourier transform
PSD	power spectral density
PQFLT	Purdue Quiet Flow Ludwieg Tube (Mach-4 Tunnel)
RMS	root-mean-square
TSP	temperature-sensitive paint

I. Introduction

A. Hypersonic Laminar-Turbulent Transition

Laminar-turbulent transition in hypersonic boundary layers is a topic of particular interest. The uncertainty in predicting the nature of transition and the great effect it has on heat transfer, skin friction, aero-optical distortion, etc. affects the design of hypersonic vehicles. Without an understanding of transition and its mechanisms, many hypersonic vehicles risk being over-designed. An inability to predict transition well causes designers to make vehicles capable of withstanding a "worst-case scenario." This generally creates heavier and more costly vehicles due to the addition of excess thermal protection. Some hypersonic missions can be pursued with acceptable risk only if transition can be better understood and better controlled.

Some of the uncertainty involved in transition prediction is because no ground-testing facility is capable of matching all aspects of flight. For example, most ground tests are performed in conventional tunnels. Conventional facilities usually have turbulent boundary layers on their nozzle walls, which radiate noise into the freestream. The noise levels of these conventional wind tunnels, defined as RMS Pitot probe fluctuations over the mean pressure, are on the order of 1%. These higher freestream noise levels can cause earlier transition than in a quiet environment, such as flight. Quiet facilities can be used to study noise effects, but do not have the capability, for example, to run at high enthalpy.

B. The Boeing/AFOSR Mach-6 Quiet Tunnel

Quiet tunnels have significantly lower noise levels than conventional wind tunnels. The freestream noise level of a quiet tunnel is about 0.1% or less.[1] The use of such tunnels to study the nature of transition provides insight into transition in a quiet, flight-like condition. Purdue University's Boeing/AFOSR Mach-6 Quiet Tunnel (BAM6QT) is one of two operational hypersonic quiet tunnels in the world. Texas A&M University houses the second, which is NASA Langley's former Mach-6 quiet tunnel.[2]

Purdue's BAM6QT was designed as a Ludwieg tube in order to reduce the cost of running the tunnel while providing high Reynolds numbers. The Ludwieg tube involves a long driver tube, a converging-diverging nozzle, test section, diffuser, burst diaphragms, and a vacuum tank (Figure 1). The tunnel is run by pressurizing the portion upstream of the burst diaphragms to a desired stagnation pressure and pumping the downstream portion to vacuum. Bursting the diaphragms starts the flow, which sends a shock wave downstream into the vacuum tank and an expansion wave upstream. The expansion wave reflects between the contraction and the upstream end of the driver tube throughout the length of the run, causing the stagnation pressure to drop quasi-statically in a stair-step fashion. In the BAM6QT's quiet configuration, air is bled from the throat of the nozzle using a fast valve (bleed valve), allowing a new boundary layer to grow on the divergent portion of the nozzle wall. The tunnel only produces quiet flow, however, if the stagnation pressure is at or below the maximum quiet pressure. To run the tunnel in a conventional configuration, the bleed valves are closed. The extended length and high polish of the nozzle allows the boundary layer to remain laminar to fairly high stagnation pressures.

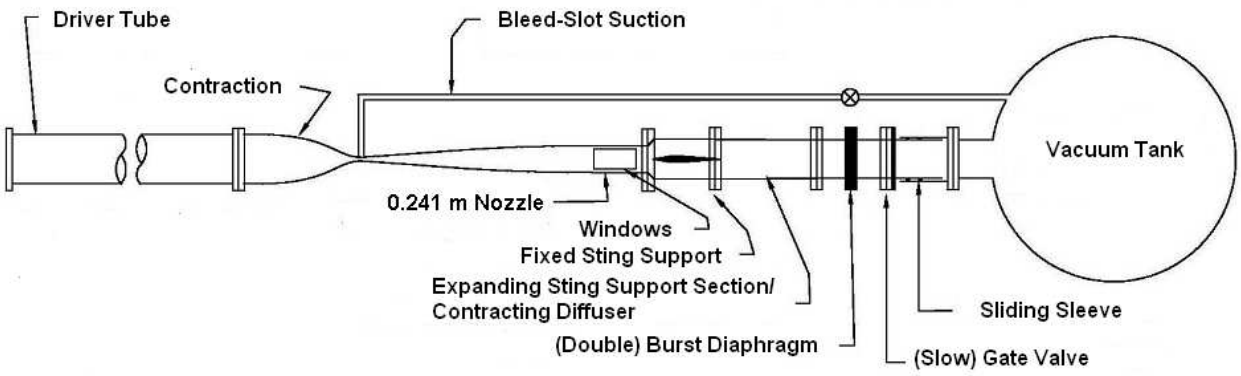

Figure 1. A schematic of the Boeing/AFOSR Mach-6 Quiet Tunnel.

1. Changes in Tunnel Performance

The BAM6QT nozzle was designed to have a maximum quiet stagnation pressure of 150 psia. In the past,[3] the maximum quiet stagnation pressure has been reported to be higher than this design pressure. When the status of quiet flow in the BAM6QT was last reported, however, the maximum quiet pressure had decreased to below 95 psia.[4] The nozzle was opened at $z = 30.265$ in. to try to determine what caused the loss of quiet flow. Small scratches were seen upon inspection, and it was determined that the throat needed to be re-polished. The polisher noted a deep scratch near $z = 10$ in, which is suspected to be from particulate impacting the nozzle wall. The re-polished nozzle was installed in early August, and after about two months of running, the BAM6QT was consistently performing with a maximum quiet pressure of about 162 psia, with very few turbulent bursts. On at least one occasion, the maximum quiet pressure has been as high as 172 psia.

2. Experiments in the BAM6QT

Some of the current experiments being performed in the BAM6QT are described here. The first experiment aims to quantify the extent of the quiet region of the tunnel using a set of pitot measurements. The second project focuses on developing a laser perturber for the BAM6QT. A third study investigates starting blunt models in the Mach-6 tunnel by varying the size of a Crew Exploration Vehicle (CEV) model. The last two experiments measure instabilities in the BAM6QT. One project focuses on crossflow transition due to distributed roughness on a 7° half-angle cone. The second looks at instabilities associated with a cylindrical roughness element on the BAM6QT nozzle wall.

II. Flow Characteristics of the BAM6QT

A. Methods to Characterize Flow in the BAM6QT

Pitot-pressure measurements were taken using a Kulite XCQ-062-15A pressure transducer to measure tunnel noise characteristics. Pressure fluctuations were measured to calculate tunnel noise levels. Mean pressure measurements were also made to find the variation of Mach number within the BAM6QT nozzle exit. All measured pressure fluctuations are normalized by the mean pressure.

Power spectra to determine root-mean-square (RMS) pressure fluctuations were calculated for 0.1-second intervals of a run. The power spectra of the fluctuations were calculated using Blackman windowing with 500 points for each fast-Fourier transform (FFT) segment and 50% overlap of the FFTs. Data presented here were sampled between 500 kHz and 2 MHz, giving a frequency resolution of 1-4 kHz. Between 199-799 FFT's were averaged for each power spectra.

Sample power spectra from a pitot-mounted Kulite sensor at around $p_{0,i} = 130$ psia are shown in Figure 2. This figure shows traces from the same sensor in quiet flow and noisy flow at similar conditions as well as a trace near vacuum (0.60 psia) with no flow. The power spectrum for the vacuum trace is normalized by the

mean pressure from the bleeds-open run. The peak seen in the quiet flow trace around 50 kHz is commonly seen in centerline measurements, but its origin is currently unknown. The resonant frequency for this Kulite is 325 kHz.

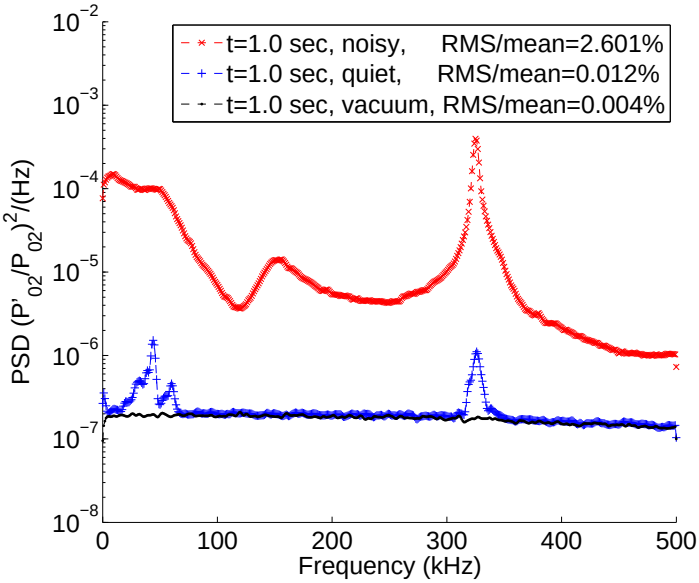

Figure 2. Sample power spectra for $z = 75.9$ in. on centerline. For quiet flow, $p_{01} = 131.1$ psia. For noisy flow, $p_{01} = 133.5$ psia. The sampling rate was 1 MHz.

The three sample spectra given in Figure 2 are integrated from 0–50 kHz. The vacuum trace gives a noise level of 0.004%, the quiet trace gives a noise level of 0.012%, and the noisy trace gives a noise level of 2.60%. The noise levels found from vacuum traces are used only for visual comparison. An upper limit of integration of 50 kHz was chosen because Kulites have a roll-off frequency near one-fifth their resonant frequency. Rather than using different integration limits for each sensor, the same upper limit was used for all measurements. The use of this limit in integration gives quiet-flow noise levels that are half the magnitude seen for full-spectrum integration (integrated to 500 kHz).

Hot films are also mounted on the nozzle wall, which provide a qualitative, non-intrusive means of determining the state of the nozzle-wall boundary layer. At high pressures, the hot films can be used to determine the BAM6QT maximum quiet pressure. Since the hot films are not calibrated, they can only be used as a qualitative indicator of noise levels.

Mach numbers were calculated using the supersonic Rayleigh pitot formula and the stagnation pressure ratio across the bow shock in front of the pitot probe. The upstream stagnation pressure was measured from a Kulite XTEL-190-500A pressure transducer, which is flush-mounted in the contraction section where the Mach number is about 0.003.[5]

B. Mapping the Extent and Uniformity of Noisy Flow

Laufer[6] found that the intensity of the radiated sound field in a supersonic wind tunnel was "uniform across the tunnel — [with] less than 1 percent variation." To check the symmetry of the BAM6QT nozzle exit under noisy flow, pitot probes were traversed in 0.25-in. increments over the upper and lower half of the BAM6QT nozzle at two different axial locations for $p_{0,i} = 90$ psia. The probe traverses only half of the vertical distance of the nozzle over the duration of the run. At each location, the probe was held stationary for 0.1 seconds so data could be gathered without effects of probe movement. During the course of each run, the boundary layer thickens due to the decrease in stagnation pressure and temperature. This effectively reduces the Mach number and increases the noise levels by a small amount as the run progresses.

The noise levels and Mach numbers from these measurements are shown in Figure 3. Figure 3 shows that the boundary layer is 1.5 in. thick on top and 1.75 in. thick on the bottom. The probe location is accurate to within 0.016 in. Additional data at 9-in. farther upstream do not show a thinner boundary layer because

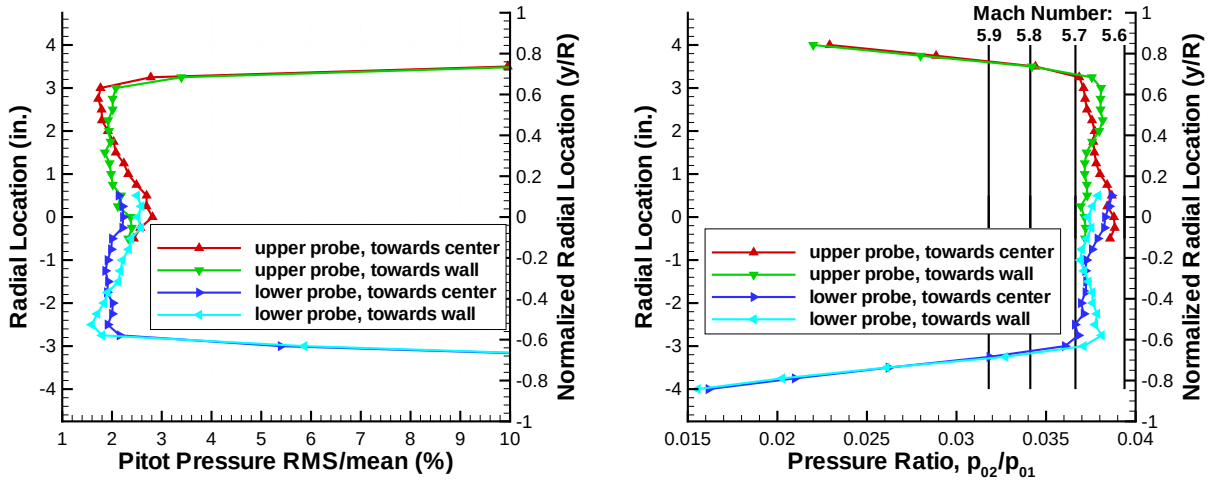

(a) Noise Levels

(b) Mach Number

Figure 3. Radial symmetry at $z = 85$ in., $p_{0,i} = 90$ psia, bleeds closed.

the change in thickness is not resolved.

The traces that traverse downward (blue, green) show a fairly uniform profile in noise level (Figure 3(a)). The noise level increases close to the centerline when the probe traverses downward. This correlation between the direction of probe movement and the noise level increase is strange since the probe is stationary for the 0.1-second increments where data are taken. The trend of higher noise at centerline, however, matches previous measurements in the former NASA Langley Mach-6 quiet tunnel (Figure 8c in Reference 7).

The Mach number uniformity in Figure 3 is similar to the noise level uniformity. There is a decrease in Mach number at centerline for probes that are traversing towards centerline (red, blue). This is expected because as the run progresses, the stagnation pressure drops, the boundary layer grows, and the effective area of the nozzle decreases. Conversely, the traces that start at centerline and traverse outwards record a Mach number that is higher on the outer edges. Data from higher stagnation pressures show similar results, with slightly higher Mach numbers. The accuracy and repeatability of these data remain to be determined.

C. Determining the Extent of Quiet Flow

Researchers in the NASA Mach 3.5 Pilot Quiet Tunnel found an axial variation of noise under quiet flow configurations within their nozzle.[8] This caused the location of boundary-layer transition on a model to be dependent on the model's axial location. To evaluate this issue in the BAM6QT, the axial variation of noise was measured.

A Dantec 55R47 hot film was installed 5.2 in. downstream of the nozzle exit. Data were taken from this hot film for bleeds-closed and bleeds-open flow and are shown in Figure 4. Each of these runs begins at $t = 0$, and start-up effects are seen for about the first half second. The bleeds-open trace shows a period of low-fluctuation flow until about $t = 2$ seconds. After this, the fluctuations increase, and the run ends at about $t = 5.7$ seconds. The bleeds-closed trace shows high fluctuations for the duration of the run, indicating a turbulent boundary layer. The bleeds-closed trace ends around $t = 9$ seconds. Tunnel run times with the bleeds closed are longer due to the lower mass flow.

These runs suggest that there is still a laminar boundary layer on the wall, 5 in. past the nozzle exit in quiet flow. This agrees with data taken in 2008,[9] which suggested that for bleeds-open flow at certain conditions, the boundary layer was laminar at $z = 5.0$ m downstream of the throat, near the downstream end of the diffuser section. Since the location of the onset of noise has not been determined, the total length of the BAM6QT uniform quiet flow core is still unknown for the first two seconds of time during bleeds-open runs. Further data has been collected by Casper,[10] who mounted Kulites into a pipe insert to collect data on pressure fluctuations on the wall downstream of the nozzle exit. Casper's data showed quiet flow about 10 in. past the nozzle exit.

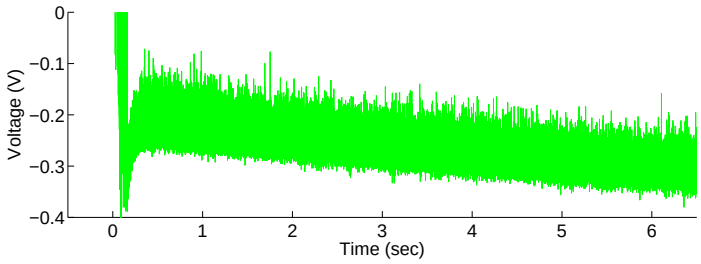

(a) Bleeds closed

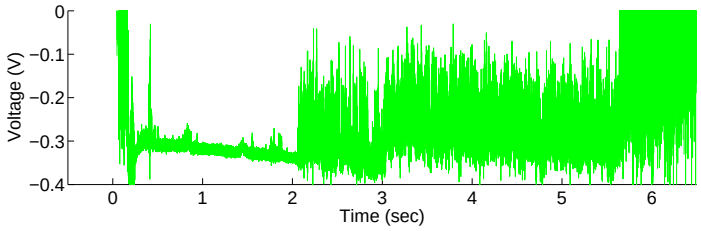

(b) Bleeds open

Figure 4. Diffuser-wall hot film at $z = 107.2$ in., $p_{0,i} = 140$ psia. Nozzle exit located at $z = 101.975$ in.

Previous findings in the BAM6QT showed that on the centerline at $p_0 = 90$ psia for $z = [84.7, 94.0]$ in., the noise levels remained low enough to be "quiet" ($p'/p < 0.05\%$) at all axial locations.[4] At about 2.2 s after the run started, noise levels were seen to increase from about 0.010% to about 0.025%. Multiple runs at $p_{0,i} = 90$ psia at various locations in the top half of the nozzle were made to study this unexplained yet repeatable noise level increase (Figure 4(b)). Reduced data from such traces are shown in Figure 5. The acoustic origins (AO) listed in the legend assume that the Mach number is 6.0. There are two key characteristics to note in Figure 5. First, the flow remains quiet at all probe locations for the first two seconds of the run. Second, the noise increases to different levels at different probe locations.

The noise levels calculated in Figure 5 were averaged for the time segment $t = [3.5, 4.5]$ s to illustrate a correlation with the acoustic origin (Figure 6). The acoustic origin was calculated based on the mean Mach number at $t = [3.5, 4.5]$ s. At about $z = 75$ in. downstream of the throat, the noise levels increase to above what is considered "quiet" flow (Figure 6). This suggests that after about two seconds of quiet flow, the onset of noise on the nozzle wall occurs at approximately $z = 75$ in. This is about 10 in. farther upstream than was predicted by computations when the nozzle was first completed, and has strong implications for where and when test-section data is usable. Measurements at $p_{0,i} = 140$ psia have shown similar results, except that the noise levels increased sooner and to slightly higher values. Further details are given in Steen's thesis work.[11]

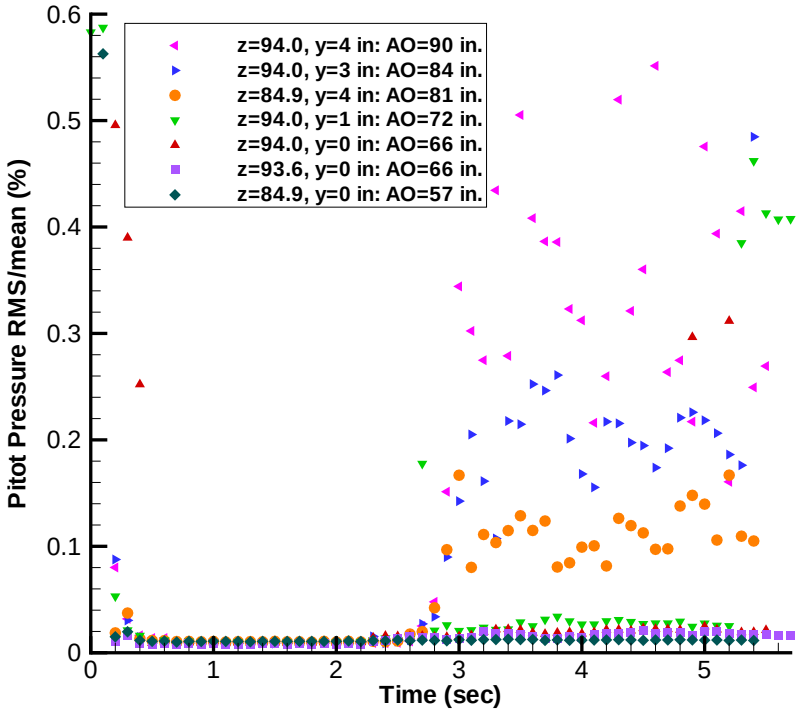

Figure 5. Noise levels for $p_{0i} = 90$ psia at various axial and radial locations for an entire run. Acoustic origins given in the legend (AO) calculated assuming $M = 6.0$.

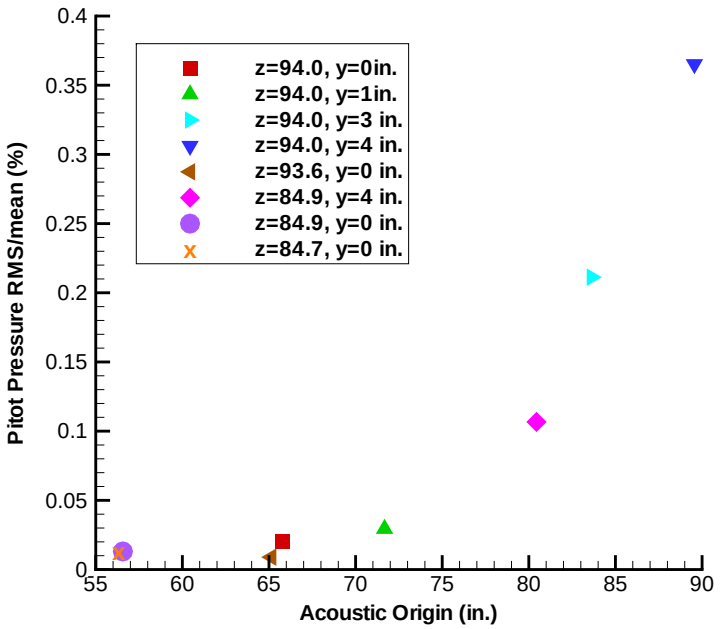

Figure 6. Averaged bleeds-open noise levels for Figure 5, $t = [3.5, 4.5]$ seconds.

III. A Laser-Induced Perturbation System for the Mach-6 Quiet Tunnel

A. Previous Work

A Spectra-Physics GCR-190 Nd:YAG laser has been used previously to create freestream perturbations in the Purdue Quiet Flow Ludwieg Tube (Mach-4 tunnel), for receptivity studies.[12–15] In these studies, a high-powered laser is focused down to a small region to increase the energy density to cause laser-induced breakdown of air. A combination of multiphoton absorption and cascade ionization occurs to ionize air molecules. A plasma core or "hot spot" is created by this process and is then used as a controlled perturbation. A weak, nearly-spherical shock emanates from this plasma core as well.

B. Laser Performance Tests

Recently, measurements were made to compare the status of the laser to its previous performance. It had not been used in about 10 years.[16] The maximum energy of the Nd:YAG laser averaged near 230 mJ/pulse, which is the same as seen by Schmisseur[12] and Salyer[13] in the late 1990s. The original Purdue Quiet Flow Ludwieg Tube (PQFLT) perturber optics were used for these performance tests.

The energy per pulse was varied to find a minimum air density at which laser perturbations could still be made. A vacuum pump was used to decrease the pressure in a test cell and then the test cell was visually inspected to see if a perturbation was created. Since these measurements were made in a test cell, the gas was assumed to be a perfect gas and the temperature was assumed to be constant. The threshold air density was inferred from the lowest pressure at which these spots could be created. Recent measurements by Chou,[17] given by the blue triangles in Figure 7, show that the threshold air density in the test cell is slightly higher than previously measured by Schmisseur[12] in 1997, given by red squares. This could be due to a number of effects such as the angle of tilt of the perturber optics with respect to the test cell window or the limited optical access in the test cell. Schmisseur and Salyer both used test cells that allowed for optical access in a direction 90° from the optical axis. The current test cell configuration allows for optical access only a few degrees off of the optical axis.

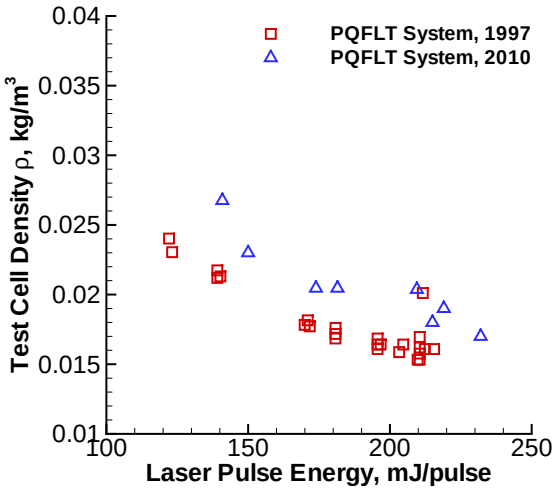

Figure 7. Comparison of threshold static density with data from Schmisseur.[12]

The time of arrival of the weak shock from the laser perturbation was also measured using PCB 132A31 sensors. These are fast pressure transducers which are manufactured as time of arrival sensors. Similar measurements made by McGuire[18] in the mid-1990s with a He-Ne deflectometer are plotted in Figure 8 as black dots. Recent measurements made by Chou matched McGuire's results to within 5%.[17]

The results of these tests show that the laser and perturber optics appear to work to the same level as seen in previous experiments. This shows that the laser is ready to be moved to the BAM6QT with a different set of perturber optics. Due to the smaller test section and therefore shorter focal length of the PQFLT perturber optics, a new perturber optics system must be designed for the Mach-6 tunnel.

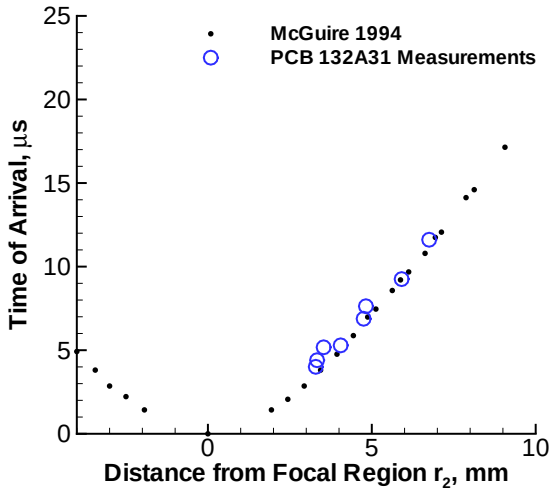

Figure 8. Comparison of time of arrival of shock measurements with data from McGuire.[18]

C. Future Work

An optical system has been designed by Steven H. Collicott to create freestream perturbations in the Mach-6 quiet tunnel.[19] The perturber optics for the Mach-6 tunnel consists of four optical elements (Figure 9). The first is an air-spaced triplet with an effective focal length of −50 mm (CVI Melles-Griot YAN-50.0-10.0), which is used to expand the beam. In order to create a higher energy density at the location where a perturbation is desired, a tighter focus is needed. This is done by decreasing the f-number of the laser beam. The second optical element in the perturber optics is a tilted cylindrical singlet with a focal length of +2000 mm. This element is used to help correct for the curvature in the tunnel windows. The last two elements are both air-spaced triplets with an effective focal length of +200 mm (CVI Melles-Griot YAP-200.0-40.0), which are used to collimate and focus the expanded laser beam. The desired perturbation is then created at the focus of this optical system. Benchtop tests will be conducted to characterize the perturbations and to compare the performance of the BAM6QT perturber optics with the PQFLT perturber optics. Hardware is also being designed to adapt the Mach-6 tunnel perturber optics to the existing BAM6QT hardware.

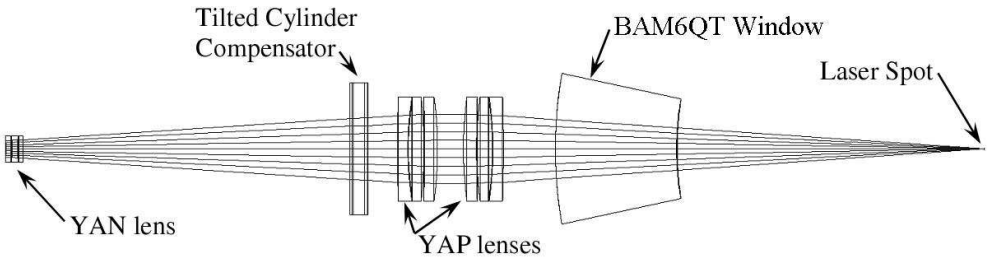

Figure 9. Perturber optics design for the Boeing/AFOSR Mach-6 Quiet Tunnel

IV. Starting Blunt Models in the Boeing/AFOSR Mach-6 Quiet Tunnel

A. Background

Models that can be started in a wind tunnel in supersonic flow are limited in both size and shape. For example, while a 5.5-in. base-diameter sharp, slender cone starts in the BAM6QT, a 2.5-in.-diameter 70° sphere-cone does not. The impingement of a shock wave on a tunnel-wall boundary layer can create an adverse pressure gradient, resulting in a region of separated flow. This effect is amplified for stronger shocks, such as the bow shock of a blunt model. Separation on the tunnel wall can then propagate far upstream through the

subsonic region of the boundary layer. Sufficiently large separation regions, coupled with model blockage, can result in a partial or total loss of supersonic flow, or tunnel "unstart." The ability to maintain flow quality and start blunt models in a wind tunnel is of great importance to the design of future hypersonic vehicles. Difficulties were encountered in tests of a 1.500-in.-diameter model of the Crew Exploration Vehicle (CEV) forebody heat shield due to model bluntness.[20] Therefore, a study was done to develop methods of starting larger blunt models in the BAM6QT.

A number of modifications have been made to the BAM6QT diffuser section in an attempt to start larger blunt models. Most recently, a straight pipe insert was installed in the diffuser section to take advantage of the sudden expansion in diameter at the junction of the nozzle exit and the upstream end of the diffuser.[21] The expansion at the nozzle exit creates an annular region between the insert and the diffuser wall. The insert, which is the same diameter as the nozzle exit and spans the length of the diffuser, is restrained coaxially in the tunnel by a set of rails. The insert can be positioned axially at increments of 0.375 in., enabling gaps of 0–1.5 in. to be formed between the nozzle exit and the upstream end of the pipe insert.

It was hypothesized that a sufficient pressure differential between the annular region and the main flow could produce enough suction to help control shock/boundary-layer interactions and prevent boundary layer separation from propagating upstream. Experiments were conducted in the BAM6QT both to verify the presence of suction through the gap and to determine methods of effectively utilizing suction to start CEV forebody heat-shield models in hypersonic flow.

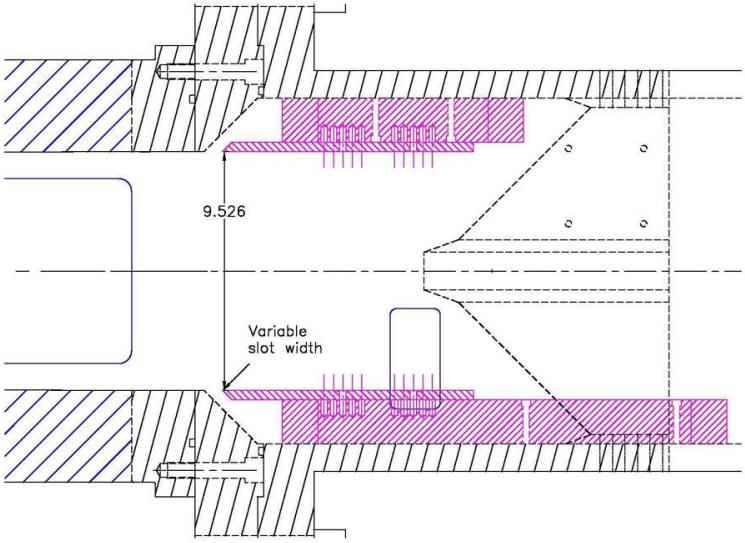

Figure 10. Schematic showing the gap created by moving the pipe insert.

B. Experimental Setup

Five Kulite pressure transducers were installed in the pipe insert section (Figure 10) at axial locations of 2, 5, and 8 in. downstream of the nozzle exit. Of the five sensors, three were model XCQ-062-15A and were positioned for static pressure measurements in the main flow and in the annular flow, and two were model XCS-093-25G and were positioned for differential measurements across the pipe insert. Calibrations were obtained for the differential Kulite sensors over the operational range using a 30 psia model 740 Paroscientific Digiquartz Laboratory Standard, which is accurate to within 0.01% of full scale. This translates to a calibration accuracy of ± 0.003 psia, which is 3-15% of the range of ΔP seen in the suction experiment and 0.050-0.075% of the range of stagnation pressures seen in the CEV starting experiment. The XCQ-062-15A and XST-190-10A absolute Kulites were calibrated using a 300 psia model 740 Paroscientific Digiquartz Laboratory Standard, which is also accurate to 0.01% of full scale. This corresponds to a calibration accuracy of ± 0.03 psi. Table 1 gives the predicted static pressures based on isentropic theory. Based on these predictions, the accuracy of the static pressure calibration is on the order of the expected static pressures for the gap suction tests. Results with Kulites in static-pressure configuration are therefore questionable.

It should be noted that the XCS-093-25G differential Kulites are rated to a differential pressure of 25 psig.

Condition	Re = 2×10^6 /ft	Re = 2.5×10^6 /ft
Quiet	0.06 psi	0.08 psi
Noisy	0.07 psi	0.10 psi

Table 1. Static pressure predictions from isentropic theory

There is therefore a risk of damaging these sensors in high-pressure tests due to the chaotic flow environment during tunnel startup. The absolute sensors have mechanical stops that prevent overpressure readings.

After the completion of the pipe-insert suction tests, CEV forebody heat-shield models were installed in the tunnel and tested. Three aluminum CEV models were used in the experiment, with diameters of 1.000, 1.250, and 1.500 in. and geometries as shown in Figure 11. The 1.500-in. CEV model was geometrically identical to the 1.500-in. CEV model described in Reference 20 that had starting issues during testing in the BAM6QT. It was believed that if the 1.500-in. model did not start even with gap suction, demonstrating that one or both of the smaller models started would provide a baseline for designing future blunt-model tests with thermal sensors. A Kulite XCQ-062-15A pressure transducer was installed in pitot configuration at the stagnation point of each model for Mach number and noise measurements. A model is said to have started if the recorded Mach number was near the tunnel's design Mach number of 6 for quiet flow and 5.8 for noisy flow. The pressure fluctuation levels also had to be on the order of 0.03% and 3% or less for quiet and noisy flow, respectively.

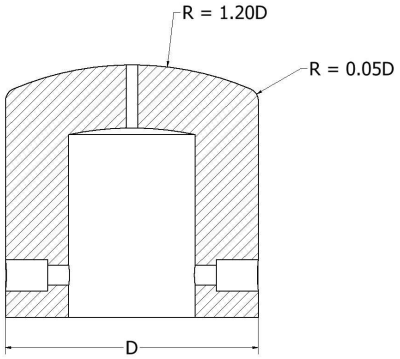

Figure 11. CEV forebody heat-shield model geometry

The model Kulite sensors were powered and amplified using custom INA-103 amplifying circuitry. Tektronix DPO7054 and TDS7104 digital oscilloscopes were used to record data. Data were sampled at 200 kHz in Hi-Res mode for the suction experiment and at 1 MHz in Hi-Res mode for the pitot measurements.

C. Results and Discussion

1. Characterization of Suction through Pipe-Insert Gap

Tests for gap suction were conducted at $Re_{\infty,i} = 2.0 \times 10^6$/ft and 2.5×10^6/ft in quiet and noisy flow with pipe-insert gap sizes of 0, 0.375, and 0.750 in. Results with the differential Kulite sensors are shown in Figure 12 for $Re_{\infty,i} = 2.0 \times 10^6$/ft ($p_{0,i} \approx 90$ psia) in quiet and noisy flow. Since the behavior of the flow field is unclear in the annular region, data from both the upstream and downstream sensors are shown in the figure. Differential pressure is shown as a function of run time, with positive Δp corresponding to higher pressure in the main flow than in the annular flow. Positive Δp in the presence of a non-zero pipe-insert gap size is likely to be an indication of suction through the gap.

In both quiet and noisy flow, the largest pressure differential is seen when the insert is mounted flush against the nozzle exit (gap size = 0 in.). It is unclear why there is a large difference between the upstream and downstream sensors, though the difference appears to be consistent from run to run. Repositioning the pipe insert for a gap of 0.375 in. results in a slight change in differential pressure. The pressure differential decreases by about 10% in the upstream sensor and increases about 10% in the downstream sensor. This

could be due to flow through a small gap around the sting mount fins. In quiet flow, the change is small compared to the zero-gap value. The measurement at the upstream sensor is about 50% of the static pressure in the main flow.

In noisy flow, the pressure differential decreases by about 50% with the increase in gap size. This larger decrease in Δp probably results from the turbulent tunnel-wall boundary layer in noisy flow versus the laminar boundary layer in quiet flow. Despite this larger decrease, the pressure differential is still about 30% of the main-flow static pressure. Since the pressure differential remains positive in the presence of the 0.375-in. gap in both quiet and noisy flow, it is likely that there is suction through the gap. Expanding the gap to 0.750 in. causes the differential pressure in both the upstream and downstream sensors to decrease to a near-zero value in quiet flow. In noisy flow, the upstream sensor indicates a positive differential pressure while the downstream sensor shows a near-zero value. These mostly negligible measurements of pressure differential indicate that a 0.750-in. gap is too large to achieve significant suction at an initial stagnation pressure of 90 psia. Tests at higher Reynolds numbers revealed similar results, with suction present for a 0.375-in. gap and a subsequent loss of suction when the gap is expanded.

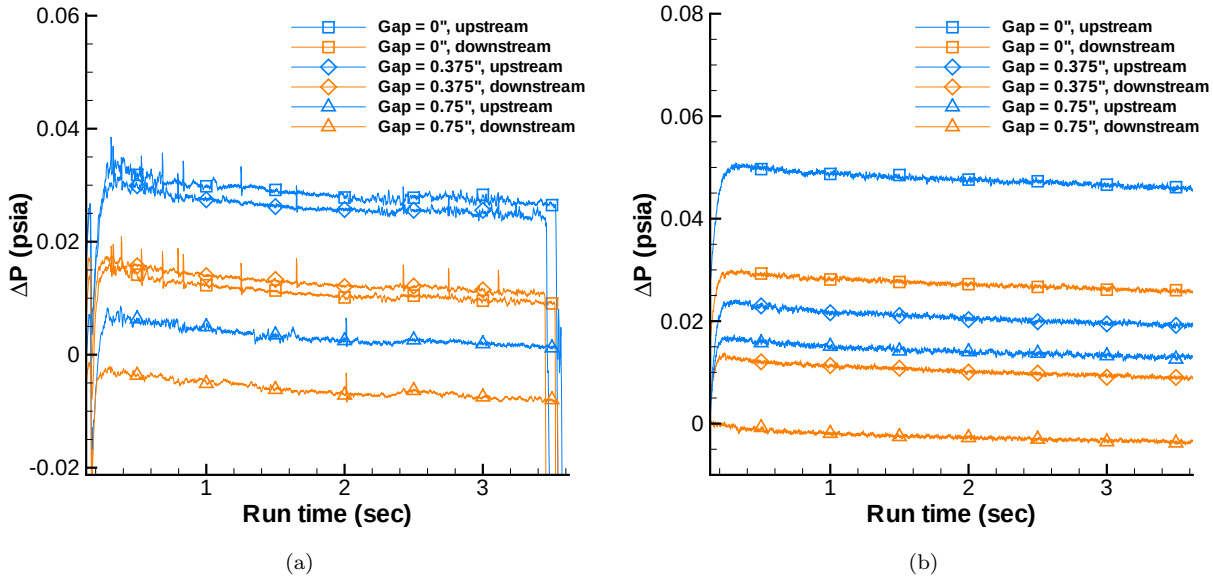

Figure 12. Differential pressure across pipe insert in upstream and downstream sensor locations at $Re_{\infty,i}$ = 2.0×10^6/ft in (a) quiet flow and (b) noisy flow

2. Starting the CEV Forebody Heat Shield in the BAM6QT

At the time of the experiment, the maximum initial stagnation pressure at which quiet flow could be maintained in the BAM6QT was about 165 psia, which corresponds to an initial free-stream unit Reynolds number of about 3.5×10^6/ft. Quiet and noisy runs were performed at this initial unit Reynolds number so that a comparison could be made between the quiet and noisy cases.

The smaller 1.000- and 1.250-in.-diameter CEV models were tested first. The models were installed with stagnation points 8.25 in. upstream of the nozzle exit plane, which is a standard location that allows the models to be seen through the downstream porthole window. For these two models, it was found that neither a gap in the pipe insert nor a specific position were needed to start the models in hypersonic flow.

Sample Mach numbers and corresponding noise measurements for quiet and noisy runs with the 1.000-in. CEV model at $Re_{\infty,i} = 3.5 \times 10^6$/ft are shown in Figure 13. Pitot data are recorded at 1 MHz and the pressure fluctuations in the RMS calculation are averaged at increments of 0.2 msec. Data in the figures begin at a run time of 0.5 seconds to avoid startup effects. The measured Mach numbers are as expected for a fully-started model: about 6.00 for quiet flow and about 5.75 for noisy flow. Noise levels for the noisy-flow run average at about 3%, which is typical for such a run. Spikes in the noise of up to 6% can be seen, though these higher noise levels are thought to result from sensor resonance at higher frequencies. Quiet-flow noise

levels, shown in green, are barely visible near 0%. Figure 14 provides a magnified view of the quiet-flow noise data. Measured quiet-flow noise levels are about 0.03%, which is typical of quiet conditions in the BAM6QT. Three turbulent bursts are also seen in the quiet run, at $t = 2.0$, 3.0, and 4.0 seconds. Results are similar for the 1.250-in. model.

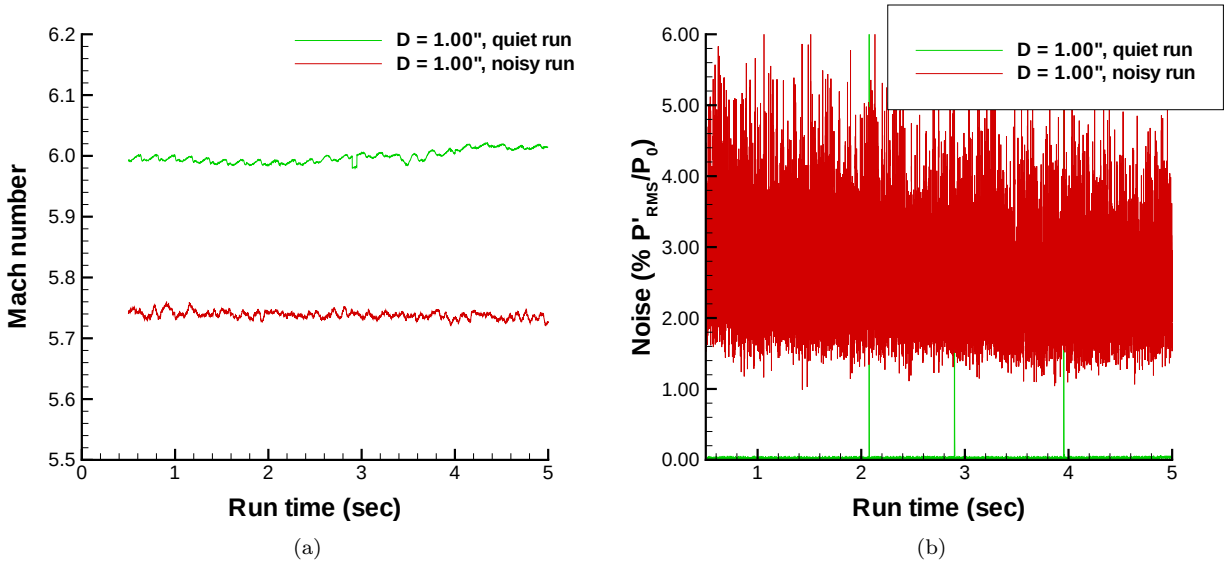

Figure 13. (a) Mach number and (b) noise measurements for the 1.000 in CEV model at $Re_{\infty,i} = 3.5 \times 10^6$/ft in quiet and noisy-flow conditions.

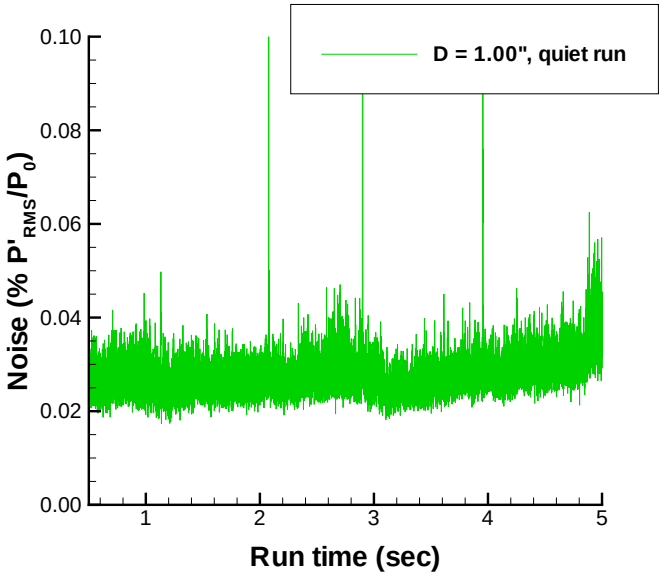

Figure 14. Magnified view of the quiet noise measurement shown in Figure 13(b)

The 1.500-in. model was installed at 8 in. upstream of the nozzle exit plane with no gap in the pipe insert. Results in quiet flow at $Re_{\infty,i} = 3.5 \times 10^6$/ft are shown in Figure 15. As expected for a started model, the measured Mach number is about 6.0 and the noise level is about 0.03%. The number of turbulent bursts is increased again with this larger model to about 6 per second. A run under noisy-flow conditions at $Re_{\infty,i} = 3.5 \times 10^6$/ft was then attempted, but resulted in a tunnel unstart.

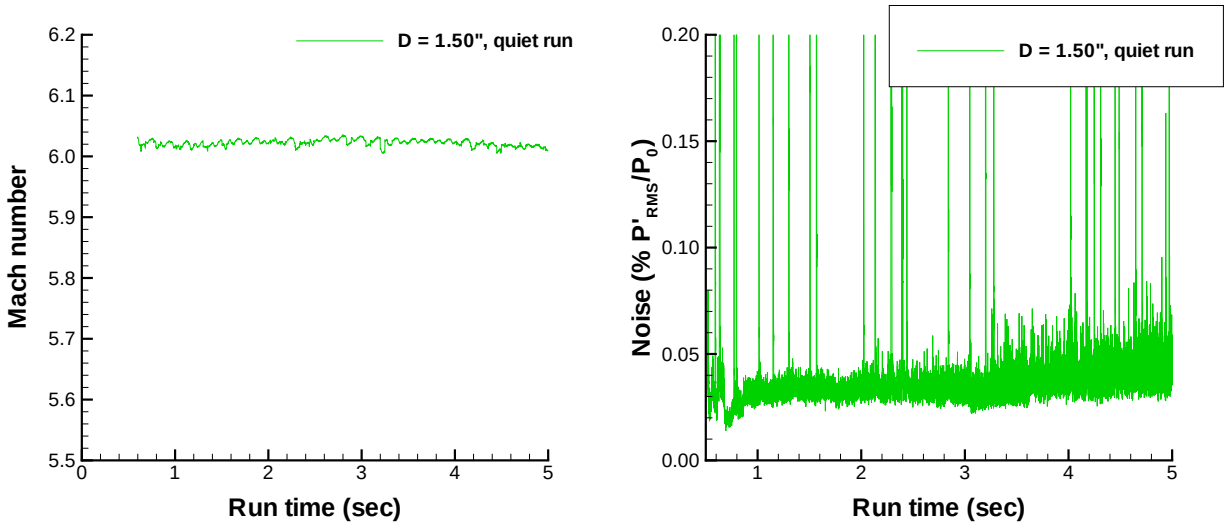

Figure 15. (a) Mach number and (b) noise measurements for the 1.500-in. CEV model at $Re_{\infty,i}$ = 3.5×10^6/ft in quiet-flow conditions.

The pipe-insert gap was then set to 0.375 in and the model was positioned based on a CFD computation for the shock-impingement location on the tunnel wall. It was desired to position the model so that the bow shock impinged within the gap. The analysis was performed by Thomas Shurtz, a Ph.D. student at Purdue University, using the OVERFLOW Flow Solver. The computation yielded a predicted tunnel-wall shock-impingement location of 9.85 in. downstream of the stagnation point under noisy-flow conditions. A total of ten streamwise model positions were tested over the range of 10.25 to 8.00 in. upstream of the nozzle exit plane, but no significant improvement in starting performance was seen. It was determined that there was insufficient suction to start the 1.500 in. model in noisy flow using the pipe-insert gap suction alone.

A test was then conducted to determine the effect of using the bleed slot suction at the throat of the nozzle in conjunction with the pipe-insert suction in starting the model in noisy flow. In order to open the bleed slot and maintain noisy flow during a run, the tunnel was pressurized above the maximum pressure at which quiet flow could be achieved. The results are shown in Figure 16 for a run at $Re_{\infty,i} = 4.3 \times 10^6$/ft with the bleeds open. From t = 0.5 to 1.5 seconds, the results are consistent with noisy-flow conditions, with a Mach number of about 5.75 and average noise levels of about 2.6%. After 1.5 seconds, the nozzle-wall boundary layer becomes laminar and the Mach number increases to a quiet-flow value of about 6.0. The noise also decreases to quiet-flow values, though there are a large number of turbulent bursts. This apparent starting in noisy flow is not an effect of the high Reynolds number, as other attempts to start the model near $Re_{\infty,i} = 5.5 \times 10^6$/ft without bleed suction were unsuccessful.[20] It is clear from Figure 16 that it is possible to start the 1.500-in. CEV model in noisy flow with the bleed slot open as long as the tunnel is initially pressurized above the maximum quiet pressure. The main disadvantage to this method of starting the model is that quiet and noisy runs cannot be directly compared, as the noisy run needs to be at a significantly higher Reynolds number than the quiet run.[22]

D. Summary

Pressure measurements were made in the pipe insert with different gap sizes and initial conditions in quiet and noisy flow. Suction was found to be present with a gap size of 0.375 in., but suction decreased for larger gap sizes. The maximum differential pressure across the pipe insert with a 0.375-in. gap was found to be about 50% of the main-flow static pressure in quiet flow and about 40% of the main-flow static pressure in noisy flow at the upstream sensor location. Increasing the Reynolds number was found to have only a minor effect on suction through the 0.375-in. gap in both quiet and noisy flow. For the 0.750-in. gap, increasing Reynolds number resulted in a small amount of suction as measured by the upstream differential sensor.

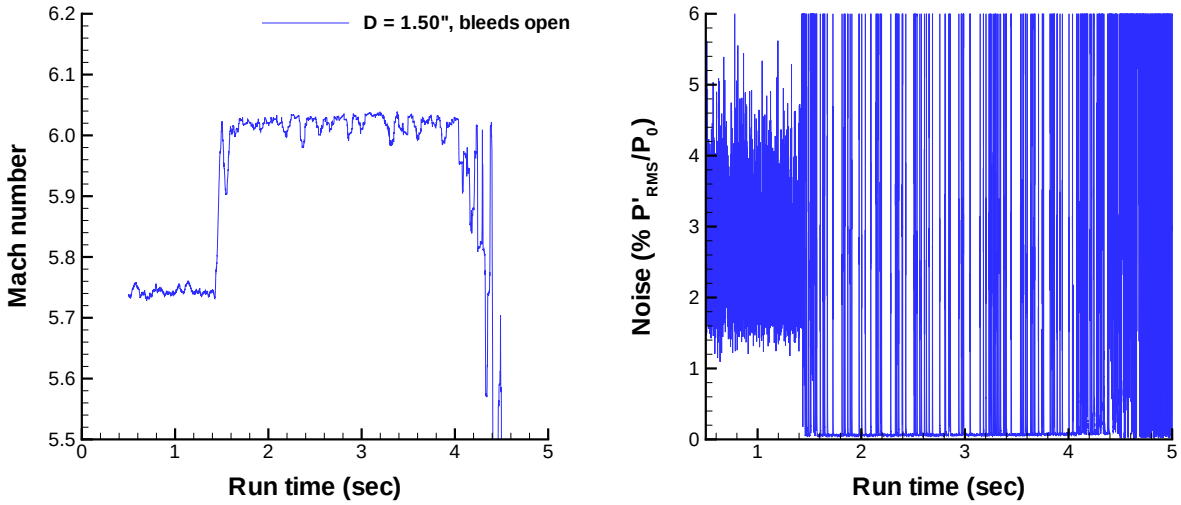

(a) (b)

Figure 16. (a) Mach number and (b) noise measurements for the 1.500-in. CEV model. Run conducted above the maximum quiet pressure, with bleeds open, at $Re_{\infty,i}$ = 4.3×10^6/ft.

Gap sizes that are much larger than 0.375 in. are unlikely to produce significant suction.

Three CEV models with diameters of 1.000, 1.250, and 1.500 in. were machined and tested in the BAM6QT to determine the effectiveness of pipe-insert suction in starting blunt models. The 1.000- and 1.250-in. models were able to start in quiet and noisy flow without aid from pipe-insert suction. The 1.500-in. model started in quiet flow, but did not start in noisy flow. An OVERFLOW computation of CEV shock shape in quiet and noisy-flow conditions was performed by Thomas Shurtz. These computations were used to position the model such that the shock impinged in or downstream of the pipe-insert gap. A total of ten model positions were tested, but the CEV did not start in noisy flow, even with suction through the pipe-insert gap. An additional test revealed that the 1.500-in. model started in noisy flow with the bleed slot open above the maximum quiet pressure.

V. Crossflow Instability and Transition on a Circular Cone at Angle of Attack

When an axisymmetric cone in hypersonic flow is pitched at an angle of attack, a circumferential pressure gradient exists due to the shock being stronger on the windward ray than the leeward ray. This circumferential pressure gradient causes the inviscid streamlines to be curved. In the boundary layer, the streamwise velocity is reduced, but the pressure gradient does not change because the static pressure is constant across the boundary layer. This imbalance between the pressure gradient and the centripetal acceleration causes a secondary flow (crossflow) in the boundary layer that is perpendicular to the inviscid streamlines. Crossflow must vanish at the edge of the boundary layer due to the balance of the centripetal acceleration and the pressure gradient. Crossflow must also vanish at the wall due to the no-slip condition. Therefore, the crossflow velocity profile has an inflection point, which is inviscidly unstable. The crossflow instability manifests itself as co-rotating vortices in the boundary layer. These vortices can be traveling or stationary. This crossflow instability is likely to be critical on many hypersonic vehicles, yet is poorly understood.

Experiments were performed on a 7° half angle cone at 6° angle of attack in the BAM6QT to measure the effect of distributed roughness on the nosetip. The cone is 40.64 cm long with a 10.16-cm base diameter (Figure 17). It includes a 15.24-cm-long nominally sharp nosetip. The frustum is painted with the temperature-sensitive paint, which in previous tests created a forward-facing step.[3,4] The new set of tests has a much reduced nosetip-frustum junction step (Table 3). These experiments were based on the work by Li et al.[23] Li showed that the neutral point of the most amplified stationary waves occur at an axial distance of roughly 5–8 cm from nosetip. In an attempt to excite these stationary waves in these current experiments,

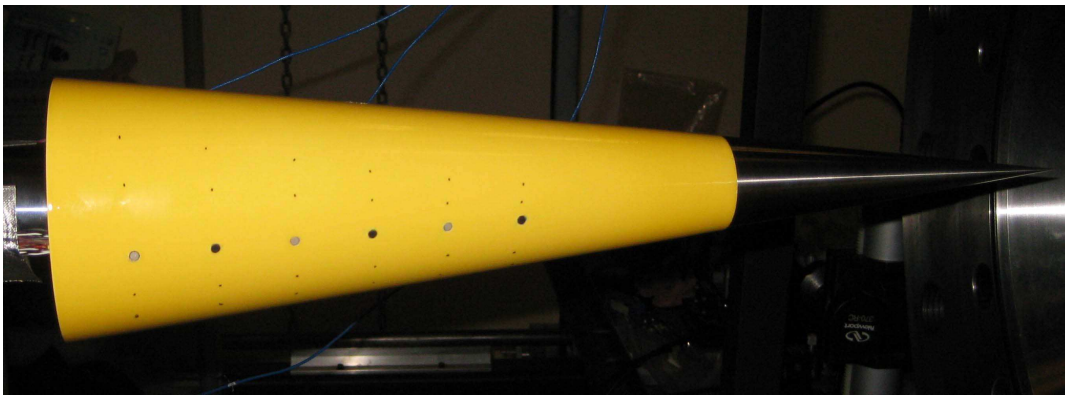

Figure 17. 7° half angle cone at 6° angle of attack with temperature-sensitive paint installed in the BAM6QT with the machine finished nosetip.

the average roughness is altered near this neutral point. In order to test the effect of distributed roughness on the crossflow instability, two nosetips were fabricated. One nosetip was left with the machine-finished surface, the other was polished to a mirror finish.

A. Instrumentation

The main instrumentation used in the crossflow instability experiments was temperature-sensitive paint (TSP). Temperature-sensitive paint is a type of luminescent paint that can be airbrushed onto a model to provide a global temperature distribution. The advantage of using TSP rather than discrete sensors, such as thermocouples, is the increased spatial resolution and the relatively low cost.[24] First the model was coated with the insulating layer. The insulating layer was composed of four coats of LustreKote white primer and four coats of LustreKote "Jet White" paint. Four coats of TSP were then applied over the insulating layer. The TSP is made of 99.95% Tris(2,22-bipyridine) dichlororuthenium(II) Hexahydrate (Ru(bpy)) dissolved in ethanol. This mixture was then combined with BASF LIMCO LC4000 Urethane Clearcoat and LIMCO LHM activator.

TSP measurement techniques involve the detection of the light intensity emitted by excited Ru(bpy) molecules. The electrons of the Ru(bpy) particles are excited by a blue LED array. Upon the electrons returning to their ground state, a red-shifted light is emitted. The intensity of this light is proportional to the temperature of the Ru(bpy) particles. The red-shifted light is recorded with a CCD camera. By comparing an image before and during a run, a ratio of the light intensity before and during a run can be determined. This light intensity ratio can then be converted to a temperature ratio. The TSP images will be presented as the number of degrees Celsius the model surface is above the initial temperature (ΔT). ΔT is qualitatively proportional to the surface heat flux. The initial model/surface temperature will also be provided for each TSP image (T_i). Ongoing work is being done to develop and refine a process of obtaining quantitative heat flux from the TSP.[25]

B. Surface Characteristics

The average roughness of the painted surface, machine finished nosetip, and polished nosetip were determined by a Mitutoyo Surftest SJ-301 profilometer. The average roughness is defined as the mean of the absolute values of the deviations from the mean height. The profilometer was traversed over a 4.0 mm length at 5 random locations and the results were averaged. These values are shown in Table 2. The painted surface and the machine-finish nosetip have a similar average roughness. The polished nosetip has an average roughness an order of magnitude less.

The magnitude of the step at the nosetip-frustum junction is documented in Table 3. These step measurements were taken at five different azimuthal locations, spaced somewhat evenly apart. Compared to previous experiments,[3,4] the magnitude of the step in the present case has been reduced by almost an order of magnitude. Note that the magnitude of the step for the present case is still about an order of magnitude greater than the average roughness of the machine-finished nosetip and two orders of magnitude greater than

Table 2. Average roughness of the painted surface, polished nosetip and machine-finished nosetip.

	Average Roughness, μm
Painted Frustum	0.28
Machine-Finished Nosetip	0.34
Polished Nosetip	0.011

the polished nosetip. The magnitude of the step is slightly different between the polished nosetip and the machine-finished nosetip. The azimuthal variations in the magnitude of the step are also significantly larger than the average roughness of both nosetips.

Table 3. Summary of the paint step at the nosetip-frustum junction for both nosetips.

	Magnitude of step at nosetip-frustum junction, μm	
	Present experiments	**Previous experiments[4, 25]**
Machine-Finished Nosetip	-5 to +4	41 to 76
Polished Nosetip	-3 to +6	43 to 82

C. Effect of Varying Distributed Roughness

Figure 18 shows two images with a unit Reynolds number of 9.3×10^6/m and either the polished or machine-finished nosetips. The two cases are qualitatively the same in that they appear to be generating the stationary vortices in the same location, visible near the leeward ray. The overall temperature distribution with the polished nosetip is slightly higher than the case with the machine-finished nosetip. This is possibly due to a difference of 7.5 K in initial model temperature. It is not clear if this surface temperature discrepancy would exist if the initial model temperature was equal. The stationary vortices appear fainter with the machine-finished nosetip, but are still originating in about the same location as with the polished nosetip. The temperature is seen on the windward ray is higher than on the leeward ray. This is most likely not due to transitional flow, but due to the thinner laminar boundary layer near the windward ray.

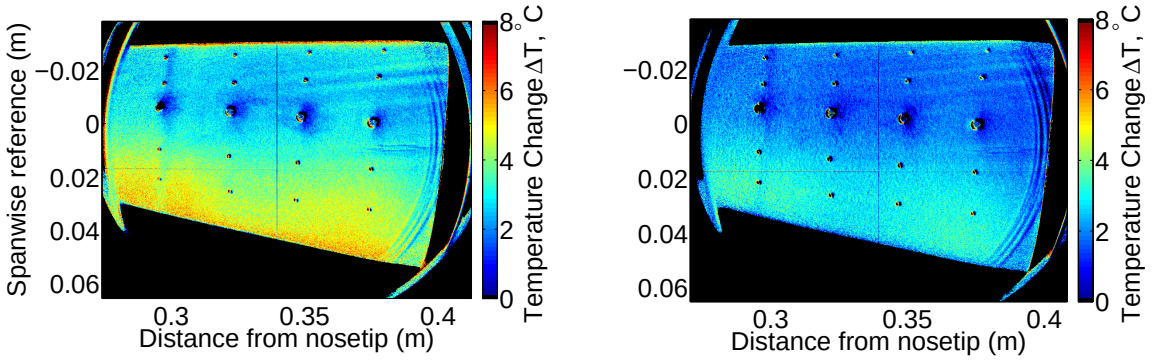

(a) Polished nosetip. p_0 = 114.2 psia, T_0 = 415.2 K, T_i = 309.3 K

(b) Machine-finished nosetip. p_0 = 113.9 psia, T_0 =416.1 K, T_i = 316.8 K

Figure 18. Temperature-sensitive paints images showing the effect of changing the distributed roughness on the nosetip under quiet flow for a unit Reynolds number of 9.3×10^6/m. Yaw side of the cone. Flow from left to right.

Figure 19 shows spanwise temperature profiles taken at an axial location of 0.36 m for both of the images in Figure 18. Six pixels were averaged in the streamwise direction for these profiles and a moving average filter was applied to the line plot. The polished nosetip case shows higher temperatures than the machine-finished nosetip case, but this may be caused by the higher initial model temperature. The temperature profiles show similar trends, with a negative slope moving away from the windward ray, and a leveling out

of the temperature near the leeward ray. The stationary vortices can be seen in the profile, although the amplitudes of the vortices are less in the machine-finished nosetip case. It appears that even though the magnitude of the nosetip-frustum paint step has been reduced significantly from the previous results,[4,25] the azimuthal variations of the step are still dominating the generation of the stationary vortices. As mentioned earlier, the magnitude along with the azimuthal variations of the step are still an order of magnitude greater than the average roughness of the machine-finished nosetip, and two orders of magnitude greater than the polished nosetip.

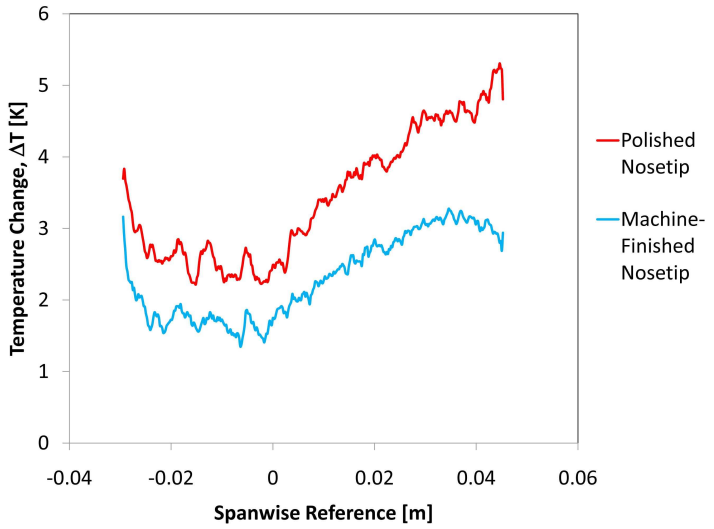

Figure 19. Spanwise temperature profiles at an axial distance of 0.36 m for both the of the images shown in Figure 18.

Another set of experiments were performed at a slightly higher Reynolds number (10.1×10^6/m) to see if an effect of the nosetip could be observed. This was the highest quiet stagnation pressure at the time (August 2010).[11] The two images with the polished and machine-finished nosetips are shown in Figure 20. For the most part, the two cases qualitatively look similar. The polished nosetip appears to be creating stationary vortices with a stronger amplitude, as inferred by the larger ΔT near the back portion of the cone. However, this increased amplitude is not convincing enough to conclude that the nosetip roughness is having a significant effect. Recall that the magnitude of the step is slightly different when the polished nosetip is installed, rather than the machine-finished nosetip.

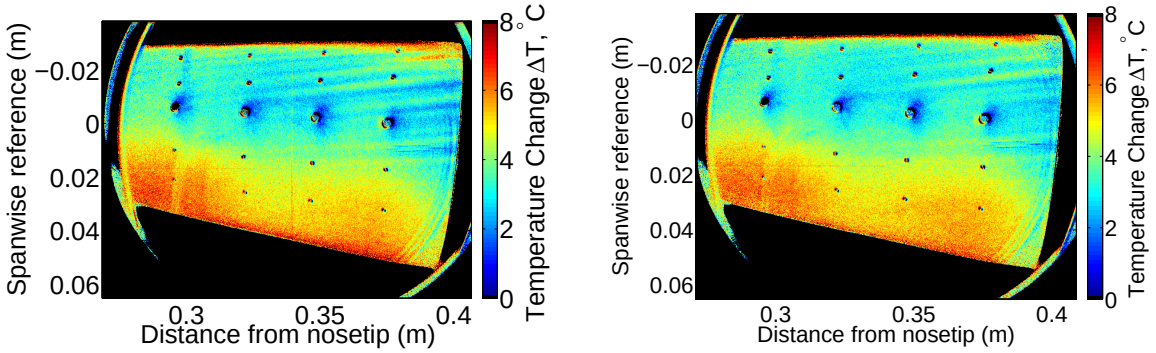

(a) Polished nosetip. p_0 = 137.9 psia, T_0 = 420 K, T_i = 304.9 K

(b) Machine-finished nosetip. p_0 = 138.1 psia, T_0 = 420 K, T_i = 304.4 K

Figure 20. Temperature-sensitive paints images showing the effect of changing the distributed roughness on the nosetip under noisy flow for a unit Reynolds number of 10.1×10^6/m. Yaw side of the cone. Flow from left to right.

Figure 21 shows the spanwise temperature profile taken at an axial location of 0.36 m from the nosetip.

The two profiles essentially fall on top of each other, and the initial model temperature is essentially the same for both cases. This plot also shows that the polished nosetip is creating stationary vortices with a slightly larger amplitude. Again, it is probably the magnitude or the azimuthal variations of the paint step that are causing the excitation of the stationary vortices, even though this step is much reduced from previous cases.

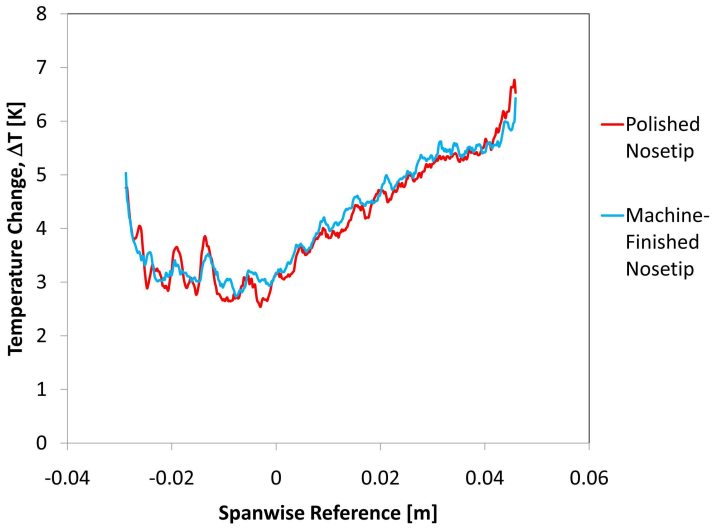

Figure 21. Spanwise temperature profiles at an axial distance of 0.36 m for both of the images shown in Figure 20.

D. Future Work

The effect of the step size needs to be reduced. New sanding techniques will be used to effectively eliminate the step by feathering the paint on the nosetip. It would also be possible to increase the roughness of the nosetips (for example by sandblasting), thus making the average roughness of the nosetip greater than magnitude of the paint edge. Future work also needs to be done to determine if the roughness is more important near the nosetip, or at some location on the frustum.

VI. Instability Measurements in the Wake of a 10.2-mm Cylindrical Roughness

A. Background

Among the many factors that can influence hypersonic transition is surface roughness. Roughness on the surface of a reentry vehicle can cause early transition and higher heating in flight.[26] Research is needed to determine if a naturally-occurring roughness will cause transition during reentry, or to determine the largest roughness that will begin to affect the natural transition location. Ideally, the growth of roughness-induced instabilities would be used to predict the location of transition.[27] A semi-empirical transition prediction method such as the e^N method might be used to reduce uncertainty in the location of transition induced by isolated roughness on hypersonic vehicles. However, these computational methods must be developed and validated with experimental measurements.

Measurements of an instability in the wake of a cylindrical roughness element have been made in the laminar nozzle-wall boundary layer of the BAM6QT.[4,21,28,29] In 2009, an instability was first detected using pitot and hot-wire probes at a frequency near 21 kHz.[29] This is believed to be the first detection of a roughness-induced instability at hypersonic speeds. To rule out stray effects from the probes, non-intrusive pressure sensors in the wake of the roughness were used to verify the existence of the instability near 21 kHz.[4] Simultaneously, Bartokowicz et al. performed numerical simulations of the roughness wake near the experimental conditions of the 21-kHz instability.[30] The computations found a disturbance of the same frequency originating from the separation region upstream of the roughness. Additional sensors were

then installed upstream of the roughness to look for the 21-kHz instability there. In addition to the 21-kHz instability, a second instability was detected at lower Reynolds numbers and higher frequencies.[4] The results here will characterize the Reynolds numbers for which each type of instability appears, for a fixed roughness height k of 10.2 mm.

B. Experimental Approach

A 5.97-mm-diameter micrometer head was mounted in a tunnel-wall insert and used as a roughness element. For these measurements, the adjustable height of the roughness was left at a constant 10.2 mm. A coordinate system for measurements will be used, where z is the axial distance from the throat, x is the spanwise distance from the center of the micrometer head at the wall, and y is the height above the wall. The roughness element was located in the nozzle of the BAM6QT at $z_0 = 1.924$ m.

Figure 22(a) shows the tunnel-wall insert with the cylindrical roughness element. The dark holes are Kulite pressure sensors that have been mounted close to the roughness element. Pressure sensors were installed at $z - z_0 = -2.0$, -1.5, and $2.0D$ (where D is the roughness diameter). The remaining holes are plugged with dowel pins. Figure 22(b) shows a photograph of the entire apparatus, looking upstream through the end of the nozzle. Additional pressure sensors were installed along the tunnel centerline at $z - z_0 = 21.9$, 46.3, 63.3, 76.1 and $93.1D$. In order to make measurements off the centerline of the roughness wake, the spanwise position of the roughness can be moved between 0.0, 0.5, 1.0, 1.5, and $2.0D$ off the tunnel centerline. The roughness is visible as a thin white line near the upstream end of the photograph. In this photograph, the roughness was placed two diameters off the tunnel centerline. A hot-film array was installed on the side wall of the nozzle and was used during each run to verify that the incoming boundary layer was laminar. Because the hot-film array was offset 90° from the roughness, it was not expected to interfere with the measurements.

Kulite XCQ-062-15A pressure transducers were used in the experiments. The Kulite XCQ-062-15A is a piezoelectric sensor with a 0.066-in. diameter, a range of 0–15 psia, and a resonance frequency near 300 kHz. The Kulites are DC sensors, so both mean and fluctuation levels can be recorded. The sensors can be used with either A- and B-screens. The A-screen has a flat dynamic response up to 30–40% of the resonance frequency while the B-screen response is flat only to 20% of the resonance frequency.[31] Due to the lesser frequency response of the B-screen sensors,[4] only A-screen sensors were used in these experiments.

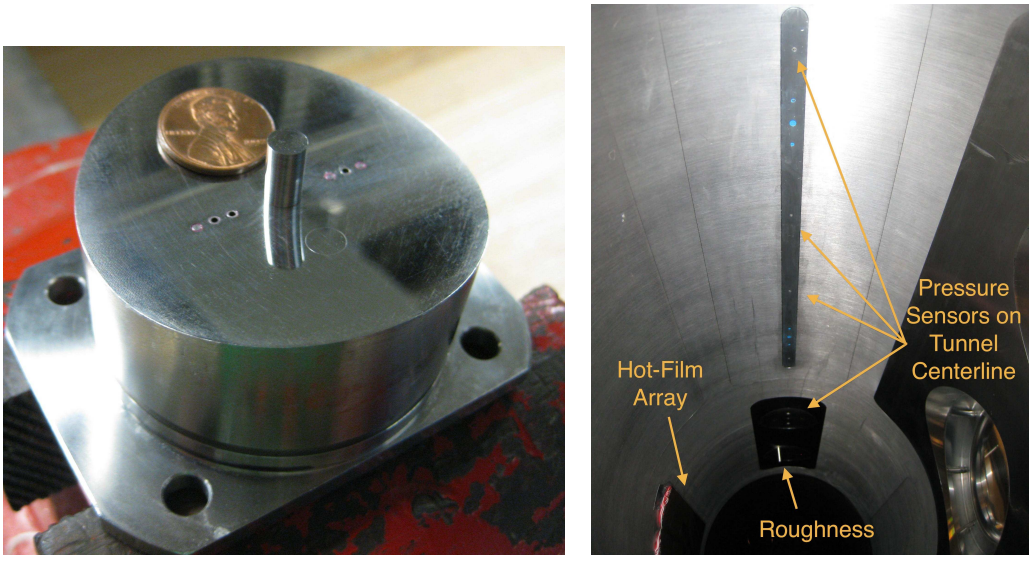

(a) Roughness insert with pressure sensors

(b) View looking upstream through nozzle

Figure 22. Roughness insert and photograph of the apparatus, looking upstream through the end of the nozzle. All pressure sensors were installed in inserts on the tunnel centerline. The roughness was moved off the tunnel centerline in order to make measurements off the center of the wake.

C. Reynolds-Number Dependency of Two Types of Instabilities for a 10.2-mm Roughness

As reported in earlier work,[4] it appears that two types of instabilities have been observed in the wake of a 10.2-mm roughness. The first instability occurs at higher Reynolds numbers (thinner nozzle-wall boundary layer) at a frequency near 21 kHz. The frequency of this instability, referred to as "Instability 1", appears to vary only slightly with Reynolds number.[29] A second instability, "Instability 2", occurs at lower Reynolds numbers (thicker boundary layer). Instability 2 has a higher frequency of 40–70 kHz, and its frequency varies greatly with Reynolds number.

The Mach-6 Tunnel has an initial stagnation temperature $T_{0,i}$ of 433 K, but can be operated at various initial stagnation pressures $p_{0,i}$ to change the freestream Reynolds number. A higher Reynolds number results in a smaller boundary-layer thickness δ, and thus a higher ratio k/δ for a fixed roughness height k. In addition, during the run the instantaneous stagnation pressure p_0 and stagnation temperature T_0 decrease quasi-statically, allowing the variation of instabilities with Reynolds number to be observed. The stagnation pressure is measured using a Kulite XTEL-190-500A pressure transducer, mounted near the contraction. The stagnation temperature is calculated from isentropic relations using the initial and instantaneous stagnation pressures.

A classic correlation parameter for transition is Re_k, the Reynolds number based on the roughness height k and conditions in the undisturbed boundary layer at the height k. Here, Re_k was calculated using boundary-layer profiles from the Harris code[32,33] and assuming Sutherland's Law for the viscosity. Figure 23 shows a plot of Re_k versus instability frequency for both types of instabilities. The data are from $21.9D$ downstream of the roughness, and 0.0–$2.0D$ off the wake centerline. The frequency at a given time is not expected to vary in the spanwise direction, but this cannot be confirmed without installing additional instrumentation. Each data point represents a different time during multiple runs with a fixed height k of 10.2 mm. The data are meant to illustrate conditions where the instability has been observed at a particular location within the wake and are not meant to be comprehensive.

The dominant instability in the wake appears to change around $Re_k = 5 \times 10^4$. Above $Re_k = 6.5 \times 10^4$, the flow is turbulent at $z - z_0 = 21.9D$, so Instability 1 may occur at higher Reynolds numbers, but farther upstream. At the time of these measurements, there were no sensors closer to the roughness. There is a 5–7 kHz scatter in frequency for Instability 2 at a given Re_k, but this may be due to errors in calculating Re_k from scaling, small variations in driver tube temperature between runs, incorrect viscosity assumptions, or a 0.25-kHz frequency resolution when calculating the spectra. This scatter results in repeatability difficulties between runs, and may explain the spanwise variation of frequencies in Figure 8 from Reference 4.

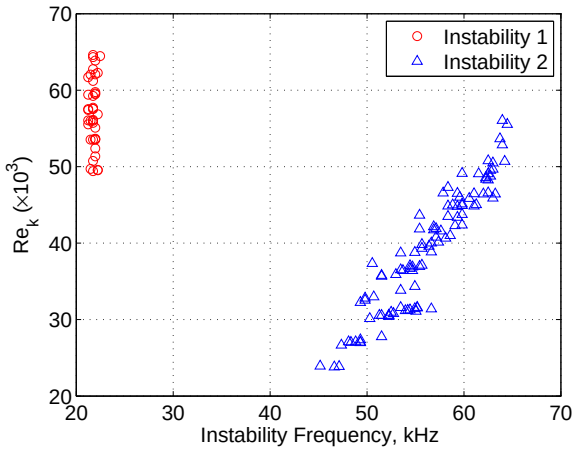

Figure 23. Re_k **versus instability frequency for both types of instabilities. Data points are from** $21.9D$ **downstream of the roughness, from multiple runs with a fixed roughness height** k**.**

D. Instabilities Detected Upstream of Roughness

The exact physical mechanisms that cause these instabilities are not fully understood. It has been thought that for these conditions, instabilities in the roughness may be either "absolute" or "convective" instabili-

ties.[26] An absolute instability would occur solely due to the roughness, such as periodic vortex shedding. A convective instability would grow downstream of the roughness in the unstable shear layer, and would be influenced by freestream disturbances interacting with the roughness wake.

Numerical simulations of the roughness found that Instability 1 occurred upstream of the roughness near a frequency of 22 kHz.[30] The computations suggested that the instability originated within the vortex structure in the separation region upstream of the roughness. It was hypothesized that unsteadiness in that region was caused by a jet of high-momentum fluid created from the strong shock in front of the roughness. As a result of these computations, an experiment was designed to place sensors upstream of the roughness and attempt to observe the instability there.

Using a sensor $1.5D$ directly upstream of the roughness, the instability was observed at conditions similar to those computed by Bartkowicz et al.[30] The instability had a frequency near 21 kHz, which is comparable to the 22 kHz seen in the computations. Figure 24 shows RMS spectra of the surface pressure fluctuations upstream of the roughness, compared to the smooth-wall laminar and turbulent spectra at similar conditions. The spectra were computed from 0.1-s time intervals with a resolution of 0.25 kHz. The pressure fluctuations are non-dimensionalized by the mean surface pressure. There were large fluctuations near 21 kHz present from Instability 1, as well as harmonics. An additional peak appears near 75 kHz which may be related to Instability 2. The fluctuations are higher than the smooth-wall turbulent levels. These measurements verify that Instability 1 is an absolute-type instability, originating upstream of the roughness as the computations suggested.

A preliminary comparison of quantitative instability amplitudes at the surface was made using the computations by Bartkowicz et al. Table 4 shows the RMS pressure fluctuations of Instability 1 at the wall, for both experiment and computations at $p_0 = 75$ psia. The RMS was calculated by integrating under the power spectrum of the pressure signal from 18–27 kHz, and was nondimensionalized by the mean pressure. Between $z - z_0 = -2.0D$ and $z - z_0 = -1.5D$, the amplitude of the instability increases by an order of magnitude, despite the fact that the sensors are close to each other. The difference between experimental and computational instability amplitudes could be due to any number of reasons. For instance, experimental amplitudes are from an average pressure signal over the sensing element while computational amplitudes are taken from a single point. Work is ongoing to improve quantitative comparisons of the instabilities.[34]

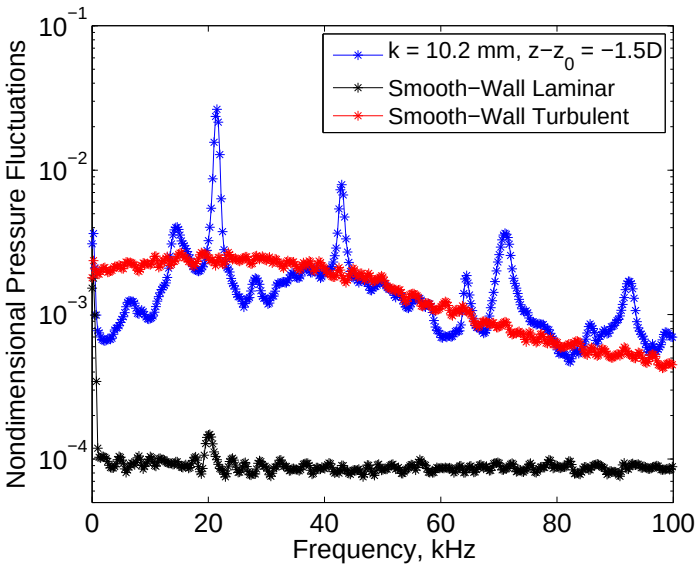

Figure 24. Instability 1 observed $1.5D$ upstream of the 10.2-mm roughness, comparable to the computations. The tunnel conditions were $p_{0,i} = 90$ psia, $p_0 = 84$ psia, and $Re_k = 6.4\times10^4$. Pressure fluctuations are non-dimensionalized by the mean pressure at the wall.

It was expected that if Instability 1 was an absolute instability, perhaps Instability 2 was a convective instability which did not appear until farther downstream. This hypothesis would have explained why the frequency of Instability 2 varies greatly with Re_k, unlike the frequency of Instability 1. However, experiments have shown that Instability 2 also appears upstream of the roughness. Figure 25 shows RMS spectra from

Table 4. Quantitative comparison of Instability 1 amplitudes upstream of the roughness. RMS amplitudes taken by integrating the area under the power spectrum of the pressure signal from 18–27 kHz. Computations by Bartkowicz et al.[30] for $p_0 = 75$ psia and experiments are from a run with $p_{0,i} = 80$ psia and $p_0 = 75$ psia.

$z - z_0$	Experiment RMS/Mean	Computation RMS/Mean
$-2.0D$	0.26%	0.46%
$-1.5D$	1.80%	3.10%

the same sensor ($1.5D$ upstream of the roughness) at five different Reynolds numbers. At Re_k greater than 5×10^4, peaks from Instability 1 can be seen near 21 kHz. However, when Re_k is reduced below 5×10^4, Instability 2 also appears upstream of the roughness. To date, Instability 2 has not been observed in the computations at the lower Reynolds numbers where it is seen in experiments.

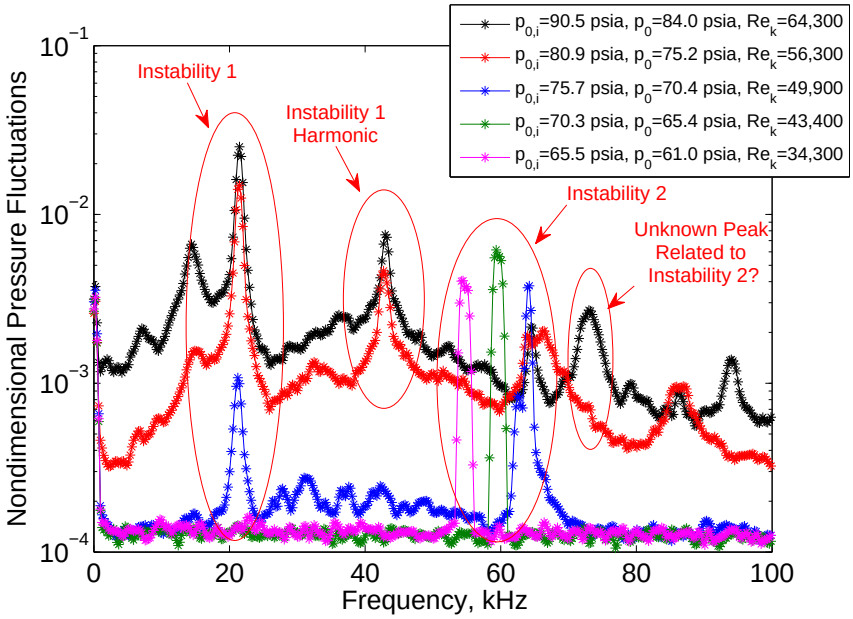

Figure 25. RMS spectra of both instabilities at five different Reynolds numbers. The pressure sensors was located $1.5D$ upstream of the roughness. Pressure fluctuations are nondimensionalized by the mean pressure at the wall.

E. Future Work

In an effort to understand the disturbance mechanisms in the wake of the roughness element, quantitative comparisons of computational/experimental instability amplitudes and frequencies are planned.[34] The ideal conditions for which to perform these detailed comparisons must be selected from a large parameter space, based on experimental and computational capabilities. Future experimental work may concentrate on searching for instabilities that occur farther downstream of the roughness.

VII. Summary

Measurements of the BAM6QT performance have been made and the development of a laser perturber system for the BAM6QT continues. The spatial extent of the uniform flow core is still unknown for about the first two seconds of the run, since the nozzle-wall boundary layer remains laminar beyond the nozzle exit. Furthermore, the pressure fluctuations for quiet flow are about 0.01% of the mean pressure, during the first two seconds of the run, at all measured locations within the nozzle. After about two seconds, measurements suggest there is an onset of noise on the nozzle wall about 75 in. downstream of the throat, from the top

half of the nozzle for $p_{0,i} = 90$ psia. The nozzle was also re-polished after several small scratches were found in the nozzle. The current maximum quiet pressure is now around $p_0 = 162$ psia. Apparatus to generate laser-induced perturbations in the BAM6QT is also being developed. The status of the laser used for the previous laser perturber was checked and its performance is similar to previous performance in the 1990s. A new optical system to be used with the BAM6QT has also been designed.

Three experiments were conducted in the BAM6QT. The first tested three different diameters of CEV models. Variations in model position and pipe insert gap were first explored to improve the starting characteristics of this model. A model diameter of 1.500 in. was able to be started in quiet flow, but required a reduction of mass flow using the tunnel bleed valves to start in noisy flow. The last two projects measured instabilities in the BAM6QT. One project looked at the effect of the nosetip roughness on the crossflow instability on a 7° half-angle cone at 6° angle of attack with TSP. Two nosetips were used, with one polished to a mirror finish. When the stationary crossflow vortices were visualized with the TSP, altering the nosetip roughness did not appear to have a large effect on the vortices. It is likely the magnitude or the azimuthal variations of the paint step at the nosetip-frustum junction was dominating the generation of the stationary vortices since little effect was seen due to nosetip roughness. In future experiments the effect of the paint step needs to be reduced allowing the effect of the nosetip roughness to be studied independently. The effect of the paint step could be reduced by minimizing the magnitude of the step or increasing the average roughness of the nosetips. The last project measured an absolute instability upstream of a roughness element in the laminar boundary layer of the nozzle wall of the BAM6QT. Additional instabilities have been found at lower Reynolds numbers. The 21 kHz absolute instability matches the one previously seen in computations.

Acknowledgments

This research is funded by AFOSR under grant FA9550-09-1-0191, NASA CUIP, the NASA Fundamental Aeronautics Program, and by an NDSEG Fellowship. The Boeing/AFOSR Mach-6 Quiet Tunnel group would also like to thank Thomas Shurtz for computations on the CEV model and Dr. Steven H. Collicott for designing the BAM6QT laser perturber system. Special acknowledgment is also due to Matt Bartkowicz for computations on the tunnel wall roughness element. Paul Thomas at American Pride Mold Polishing once again did an outstanding job of polishing the nozzle throat.

References

[1]Beckwith, I. E. and Miller, III, C. G., "Aerothermodynamics and Transition in High-Speed Wind Tunnels at NASA Langley," *Annual Review of Fluid Mechanics*, Vol. 22, January 1990, pp. 419–439.

[2]Hofferth, J., Bowersox, R., and Saric, W., "The Texas A&M Mach 6 Quiet Tunnel: Quiet Flow Performance," AIAA Paper 2010–4794, June 2010.

[3]Berridge, D. C., Chou, A., Ward, C. A. C., Steen, L. E., Gilbert, P. L., Juliano, T. J., Schneider, S. P., and Gronvall, J. E., "Hypersonic Boundary-Layer Transition Experiments in a Mach-6 Quiet Tunnel," AIAA Paper 2010-1061, January 2010.

[4]Ward, C. A. C., Wheaton, B. M., Chou, A., Gilbert, P. L., Steen, L. E., and Schneider, S. P., "Boundary-Layer Transition Measurements in a Mach-6 Quiet Tunnel," AIAA Paper 2010-4721, June 2010.

[5]Borg, M. P., *Characteristics of the Contraction of the Boeing/AFOSR Mach-6 Quiet*, Master's thesis, School of Aeronautics and Astronautics, Purdue University, West Lafayette, IN, December 2005.

[6]Laufer, J., "Aerodynamic Noise in Supersonic Wind Tunnels," *Journal of the Aerospace Sciences*, Vol. 28, No. 9, 1961, pp. 685–692.

[7]Blanchard, A. E., Lachowicz, J. T., and Wilkinson, S. P., "NASA Langley MAch-6 Quiet Wind-Tunnel Performance," *AIAA Journal*, Vol. 35, No. 1, 1997, pp. 23–28.

[8]Beckwith, I. E., Creel, Jr., T. R., Chen, F.-J., and Kendall, J. M., "Free-Stream Noise and Transition Measurements on a Cone in a Mach 3.5 Pilot Low-Disturbance Tunnel," NASA, TP 2180, 1983.

[9]Juliano, T. J., Segura, R., Borg, M. P., Casper, K., Hannon, M. J., Wheaton, B. M., and Schneider, S. P., "Starting Issues and Forward-Facing Cavity Resonance in a Hypersonic Quiet Tunnel," AIAA Paper 2008-3735, June 2008.

[10]Casper, K., Beresh, S., and Schneider, S., "Pressure Fluctuations Beneath Turbulent Spots in a Hypersonic Boundary Layer," AIAA Paper to appear, January 2011.

[11]Steen, L. E., *Characterization and Development of Nozzles for a Hypersonic Quiet Wind Tunnel*, Master's thesis, Purdue University, West Lafayette, IN, December 2010.

[12]Schmisseur, J. D., *Receptivity of the Boundary Layer on a Mach-4 Elliptic Cone to Laser-Generated Localized Freestream Perturbations*, Ph.D. thesis, School of Aeronautics and Astronautics, Purdue University, West Lafayette, IN, December 1997.

[13]Salyer, T. R., *Laser Differential Interferometry for Supersonic Blunt Body Receptivity Experiments*, Ph.D. thesis, School of Aeronautics and Astronautics, Purdue University, West Lafayette, IN, May 2002.

[14]Ladoon, D. W., Schneider, S. P., and Schmisseur, J. D., "Physics of Resonance in a Supersonic Forward-Facing Cavity," *Journal of Spacecraft and Rockets*, Vol. 35, No. 5, Sep-Oct 1998, pp. 626–632.

[15]Schmisseur, J. D., Collicott, S. H., and Schneider, S. P., "Laser-Generated Localized Freestream Perturbations in Supersonic and Hypersonic Flows," *AIAA Journal*, Vol. 38, No. 4, April 2000, pp. 666–671.

[16]Salyer, T. R., "Characterizing Laser-Generated Hot Spots for Receptivity Studies," *AIAA Journal*, Vol. 44, No. 12, December 2006, pp. 2871–2878.

[17]Chou, A., *Characterization of Laser-Induced Perturbations and Instability Measurements on a Flared Cone*, Master's thesis, School of Aeronautics and Astronautics, Purdue University, West Lafayette, IN, December 2010.

[18]McGuire, J. B., *Fluid Dynamic Perturbations using Laser Induced Breakdown*, Master's thesis, School of Aeronautics and Astronautics, Purdue University, West Lafayette, IN, August 1994.

[19]Collicott, S. H., "Initial Mach 6 LT Spot Maker Design Summary," Unpublished report, Purdue University, West Lafayette, IN, August 2010, 7 pages.

[20]Gilbert, P. L., *Effect of Tunnel Noise on Laminar Stagnation-Point Heating at Mach 6*, Master's thesis, Purdue University, West Lafayette, IN, December 2010.

[21]Wheaton, B. M., Juliano, T. J., Berridge, D. C., Chou, A., Gilbert, P. L., Casper, K. M., Steen, L. E., Schneider, S. P., and Johnson, H. B., "Instability and Transition Measurements in the Mach-6 Quiet Tunnel," AIAA Paper 2009-3559, June 2009.

[22]Gilbert, P. L., "Investigation of Downstream Suction and Starting Blunt Models in the Boeing/AFOSR Mach-6 Quiet Tunnel," Unpublished memo, Purdue University, December 2010, 22 pages.

[23]Li, F., Choudhari, M., Chang, C.-L., and White, J., "Analysis of Instabilities in Non-Axisymmetric Hypersonic Boundary Layers over Cones," AIAA Paper 2010-4643, June 2010.

[24]Liu, T. and Sullivan, J. P., *Pressure and Temperature Sensitive Paints*, Springer, 1st ed., 2005.

[25]Ward, C. A. C., *Hypersonic Crossflow Instability and Transition on a Circular Cone at Angle of Attack*, Master's thesis, Purdue University, West Lafayette, IN, December 2010.

[26]Schneider, S. P., "Effects of Roughness on Hypersonic Boundary-Layer Transition," *Journal of Spacecraft and Rockets*, Vol. 45, No. 2, March-April 2008, pp. 193–209.

[27]Klebanoff, P. S. and Tidstrom, K. D., "Mechanism by Which a Two-Dimensional Roughness Element Induces Boundary-Layer Transition," *The Physics of Fluids*, Vol. 15, No. 7, July 1972, pp. 1173–1188.

[28]Wheaton, B. M., *Roughness-Induced Instability in a Laminar Boundary Layer at Mach 6*, Master's thesis, Purdue University School of Aeronautics & Astronautics, West Lafayette, IN, December 2009.

[29]Wheaton, B. M. and Schneider, S. P., "Roughness-Induced Instability in a Laminar Boundary Layer at Mach 6," AIAA Paper 2010-1574, January 2010.

[30]Bartkowicz, M. D., Subbareddy, P. K., and Candler, G. V., "Numerical Simulations of Roughness Induced Instability in the Purdue Mach 6 Wind Tunnel," AIAA Paper 2010-4723, June 2010.

[31]Beresh, S. J., Henfling, J. F., Spillers, R. W., and Pruett, B. O. M., "Measurement of Fluctuating Wall Pressures Beneath a Supersonic Turbulent Boundary Layer," AIAA Paper 2010-0305, January 2010.

[32]Harris, J. E. and Blanchard, D. K., "Computer Program for Solving Laminar, Transitional, or Turbulent Compressible Boundary-Layer Equations for Two-Dimensional and Axisymmetric Flow," NASA Technical Report TM-83207, February 1982.

[33]Schneider, S. P., "Design of a Mach-6 Quiet-flow Wind Tunnel Nozzle using the e**N Method for Transition Estimation," AIAA Paper 1998-0547, January 1998.

[34]Wheaton, B. M., Schneider, S. P., Bartkowicz, M. D., Subbareddy, P. K., and Candler, G. V., "Numerical and Experimental Comparison of Roughness-Induced Instabilities at Mach 6," Submitted to 41st AIAA Fluid Dynamics Conference and Exhibit, Honolulu, HI, June 2011.